ACS APPLIED MATERIALS & INTERFACES

Research Article

www.acsami.org

Electrospun ZnO Nanowire Plantations in the Electron Transport Layer for High-Efficiency Inverted Organic Solar Cells

Naveen Kumar Elumalai,[†,‡,§,∥] Tan Mein Jin,[†,‡,§] Vijila Chellappan,*[,§] Rajan Jose,*[,⊥] Suresh Kumar Palaniswamy,[#] Sundaramurthy Jayaraman,[∥] Hemant Kumar Raut,[‡,§,∥] and Seeram Ramakrishna[‡,∥]

[‡]National University of Singapore, Singapore 117576

[§]Institute of Materials Research and Engineering (IMRE), Agency for Science, Technology and Research (A*STAR), 3 Research Link, Singapore 117602

[⊥]Faculty of Industrial Sciences & Technology, Universiti Malaysia Pahang, 26300 Kuantan, Pahang, Malaysia

[#]Environmental & Water Technology, Centre of Innovation, Ngee Ann Polytechnic, Singapore

[∥]Center for Nanofibers and Nanotechnology, National University of Singapore, Singapore

Supporting Information

ABSTRACT: Inverted bulk heterojunction organic solar cells having device structure ITO/ZnO/poly(3-hexylthiophene) (P3HT):[6,6]-phenyl C61 butyric acid methyl ester (PCBM) /MoO_3/Ag were fabricated with high photoelectric conversion efficiency and stability. Three types of devices were developed with varying electron transporting layer (ETL) ZnO architecture. The ETL in the first type was a sol−gel-derived particulate film of ZnO, which in the second and third type contained additional ZnO nanowires of varying concentrations. The length of the ZnO nanowires, which were developed by the electrospinning technique, extended up to the bulk of the photoactive layer in the device. The devices those employed a higher loading of ZnO nanowires showed 20% higher photoelectric conversion efficiency (PCE), which mainly resulted from an enhancement in its fill factor (FF). Charge transport characteristic of the device were studied by transient photovoltage decay and charge extraction by linearly increasing voltage techniques. Results show that higher PCE and FF in the devices employed ZnO nanowire plantations resulted from improved charge collection efficiency and reduced recombination rate.

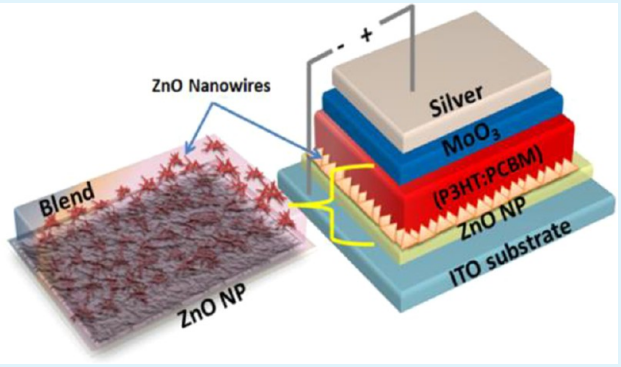

KEYWORDS: *renewable energy materials, charge transport layers, inverted polymer solar cells, heirarchical structures, carrier lifetime, electrospinning*

INTRODUCTION

Organic solar cells (OSCs) have attracted considerable interest as a potential renewable energy device because they can be prepared at lower cost, with lower environmental load and flexibility, and are lightweight compared to the conventional silicon solar cells.[1,2] The photoactive layer of OSCs consists of a p-conjugated polymer as an electron donor and a fullerene derivative as an electron acceptor. A large number of stable conjugated polymers at atmospheric conditions are proposed for efficient and stable OSCs.[3−6] Because of their acceptable hole and electron conductivities, desirable optical absorption cross-section, and atmospheric stability, the poly3-hexylthiophene (P3HT): l-3-methoxycarbonylpropyl-L-phenyl-6,6 methanofullerene (PCBM) conjugate has emerged as one of the popular choices to build high-efficiency OSCs. Recent advances in developing new organic active layer materials and device-processing techniques have led to improvement in photoelectric conversion efficiencies (PCE) exceeding ∼10%.[7,8]

The P3HT:PCBM photoactive layer is sandwiched between two electrodes comprising an indium tin oxide (ITO) coated with poly(3,4-ethylenedioxythiophene)−poly(styrene sulfonate) (PEDOT:PSS) (anode) and a low work function metal, typically Al and Ag (cathode) in OSCs. However, operational stability of the above devices is poor under ambient conditions for practical applications because of many complex processes in the photoactive as well as other functional layers.[9] To address the stability issues, inverted OSCs (IOSCs)[10−14] are proposed. In IOSCs, electrons are collected at the ITO side by coating it with an n-type metal oxide semiconductor (MOS), which serve

Received: April 16, 2013
Accepted: September 12, 2013
Published: September 12, 2013

as an electron transport layer (ETL), and the holes collection are facilitated by a hole transport layer (HTL), typically a high work function metal. High efficiency IOSCs employs TiO_2, ZnO, ReO etc. as ETL[15−17] and metals of higher corrosion and oxidation resistances such as Ag and Au are as HTL. One of the ideal ETL material is ZnO owing to its low work function, high electron mobility, high optical transparency, and environmental stability.[18] High PCE ∼4.2% are reported for IOSCs using ZnO as an ETL.[18] Several research groups have reported IOSCs employing various forms of ZnO such as nanoparticles, nanorods, and uniform films as ETLs.[6,8,9,19−21]

One of the primary factors reducing the performance parameters of IOSCs is the inferior charge collection efficiency due to increased charge recombination at the photoactive layer as well as at its interface with the buffer layers. Recombination at the photoactive layer occurs because of inferior charge mobility (electron mobility μ_e ∼5−7 × 10^{-4} $cm^2/(V\ s)$, hole mobility μ_h ∼0.5−9 × 10^{-4} $cm^2/(V\ s)$) arise from highly disordered molecular arrangement in polymers and incoherent charge hopping thereby.[22−24] Inferior electrical conductivity of the nanostructured MOS charge transport layers and consequent carrier build up at the photoactive−buffer layer interface is one another source of recombination.[25] Morphologies of the photoactive and the transport layers are shown to have a major role in charge carrier transport and affect the device performance significantly.[26−28]

Recent studies show that electron conducting nanowires on the ETL with their length reaching to most of the photoactive layer (P3HT: PCBM) thickness improves charge collection efficiency.[26,29−31] In the case of IOSCs, these attempts include fabrication of ZnO nanorods using hydrothermal and pulsed current electrolysis methods with a PCE up to ∼2.7%.[29,30] We have now significantly improved the PCE of IOSCs up to ∼3.5% by planting electrospun ZnO nanowires onto ETLs. Rationale of using electrospun nanowires is that they can support high electron diffusivity and mobility, which would enhance the charge collection efficiency, and can be tailored by controlling the crystallinity.[32−36] The devices that employed electrospun ZnO nanowires gave up to ∼20% higher PCE than control devices that did not employ them. The enhanced PCE resulted from an increase in the fill factor; and therefore, the electrospun ZnO nanowires reduce the charge recombination rate and improve the collection efficiency. The charge transport through these devices were studied by transient photovoltage decay and charge extraction by linearly increasing photovoltage measurement techniques and observed that the devices employing electrospun nanowires are characterized by high electron lifetime and mobility.

2. EXPERIMENTAL DETAILS

2.1. Preparation of ZnO Sol−Gel Thin Films on ITO. Zinc acetate dihydrate [$Zn(CH_3COO)_2{\cdot}2H_2O$, ZnAc; Alfa Aesar, 99.9%], potassium hydroxide (KOH; Merck, 85%), ethanolamine ($NH_2CH_2CH_2OH$, EA, Sigma Aldrich, 99.5%, 0.15 g) in 2-methoxyethanol ($CH_3OCH_2CH_2OH$, ME, Aldrich, 99.8%, 5 mL) were the starting materials. The ZnAc (0.6 g) and EA (0.15 g) were dissolved in ME (5 mL) under vigorous stirring for 24 h in air. Ammonia (1 mL) was then added to the above solution and stirred for 2h to get a sol and then filtered using 0.25 μm PVDF filter to remove insoluble impurities. The ZnO thin films (∼40 nm) were produced by spin coating the above sol onto cleaned ITO substrates at 3500 rpm for 90 s. The films were then annealed at 160 °C in air for 3 h, cooled to room temperature, washed mildly with isopropyl alcohol, and then dried in air.

2.2. Preparation of ZnO Nanowire Plantations. Free standing ZnO nanowires were produced by electrospinning technique.[37] In the typical synthesis procedure, zinc acetate dihydrate [$Zn(CH_3COO)_2{\cdot}2H_2O$], polyvinylpyrolidone (PVP, MW: 130000) and acetic acid (99.7%) were purchased from Aldrich and used without any further purification. In a typical synthesis, homogeneous sol−gel solution was prepared by mixing 1.5 g of PVP in 15 mL of ethanol and then stirred for 1 h in room temperature. Further, the prepared homogeneous polymer solution is mixed with 2.2g of zinc acetate solution under constant stirring for an hour. Finally, 0.8 mL of acetic acid was added to the solution under vigorous stirring for ∼12 h in room temperature. The prepared sol−gel solution was then transferred into a 5 mL syringe (diameter of 11.9 mm) with 181/2 G stainless steel needle which has a diameter of 0.084 cm. The humidity level of the synthesis electrospinning chamber was maintained at about 35% for the whole experimental process. The distance between needle and static collector (aluminum foil) was maintained at 10 cm with an applied ac voltage of 20 kV and at a flow rate of 1 mL/h using a syringe pump (KDS 200). Finally, the prepared composite fibers were collected and further sintered at 500 °C for 5 h under air atmosphere, with a heating ramp rate of 5 °C min to yield ZnO nanowires.

The electrospun ZnO nanowire plantations were prepared as follows. First, the sol−gel precursor was spun coated onto ITO substrate and then annealed for 10 min at 70 °C. Subsequently an ethanolic suspension containing electrospun ZnO nanowires were spin coated onto the annealed substrate. Two typical concentrations were prepared (i) a higher concentration containing 5 mg of nanowires in 5 mL of ethanol and spin-coated at 2000 rpm (PNW_H film) (ii) a lower concentration of 1 mg of nanowires in 5 mL of ethanol and spin-coated at 4000 rpm (PNW_L film).

Crystal structure of the ZnO films and electrospun nanowires was studied by X-ray diffraction using Bruker General Area Detector Diffraction System (GADDs) employing CuKα target and 2D detector. Morphologies of the ZnO films on ITO and electrospun wires were studied by field-emission scanning electron microscope (JEOL FEG JSM 6700F) operating at 10 kV. High-resolution lattice images and selected area diffraction patterns (SAED) were obtained using transmission electron microscope (TEM) operating at 300 kV (FEI, Titan 80−300 kV).

2.3. Device Fabrication and Testing. All the above dried films were cleaned by UV-Ozone treatment for 10 min before solar cell fabrication. The device structure was ITO/ZnO/P3HT: PCBM/MoO_3/Ag. Three types of devices were fabricated viz. (i) the sol gel film is termed as "device P", (ii) the low and (iii) high concentration of ZnO nanowire plantations protruding are termed as "device PNW_L" and "device PNW_H", respectively. Typically three devices were fabricated in each type. A mixture of P3HT and PCBM dissolved in the ratio of 1:0.8 in 1,2-dichlorobenzene solution was spin coated on the ITO/ZnO layer. The thickness of the photoactive layer was ∼200 nm. The film was then annealed at 240 °C for 10 min. The hole transporting MoO_3 layer of thickness ∼5 nm was then thermally evaporated on to the produced film in a vacuum chamber with a base pressure of ∼1 × 10^{-7} mbar. Finally, silver (∼100 nm) electrode was deposited onto the MoO_3 layer at a pressure ∼1 × 10^{-5} mbar. The devices were annealed at 70 °C for 10 min using a hot plate inside the nitrogen filled glovebox. Surface roughness and nanowire distribution were studied by atomic force microscopy (AFM). AFM images are recorded with Bruker's Dimension Icon equipment operated in tapping mode at ambient conditions.

The devices were then cooled to room temperature and undertook photocurrent measurements using a source meter (Keithley 2400, USA) at AM1.5G illumination employing a solar simulator (SAN-EI Electric XES-301S, Japan). IPCE measurements were performed on a Stanford Research 830 lock-in amplifier integrated with a Newport 150 W xenon white light lamp through a 237 Hz mechanical chopper wheel and Cornerstone monochromator (130 1/8 m).

2.4. Evaluation of Carrier Recombination and Mobility. The carrier lifetime and recombination dynamics was determined by transient photovoltage (TPV) measurements. The TPV experiments were conducted by connecting the devices to a high input impedance

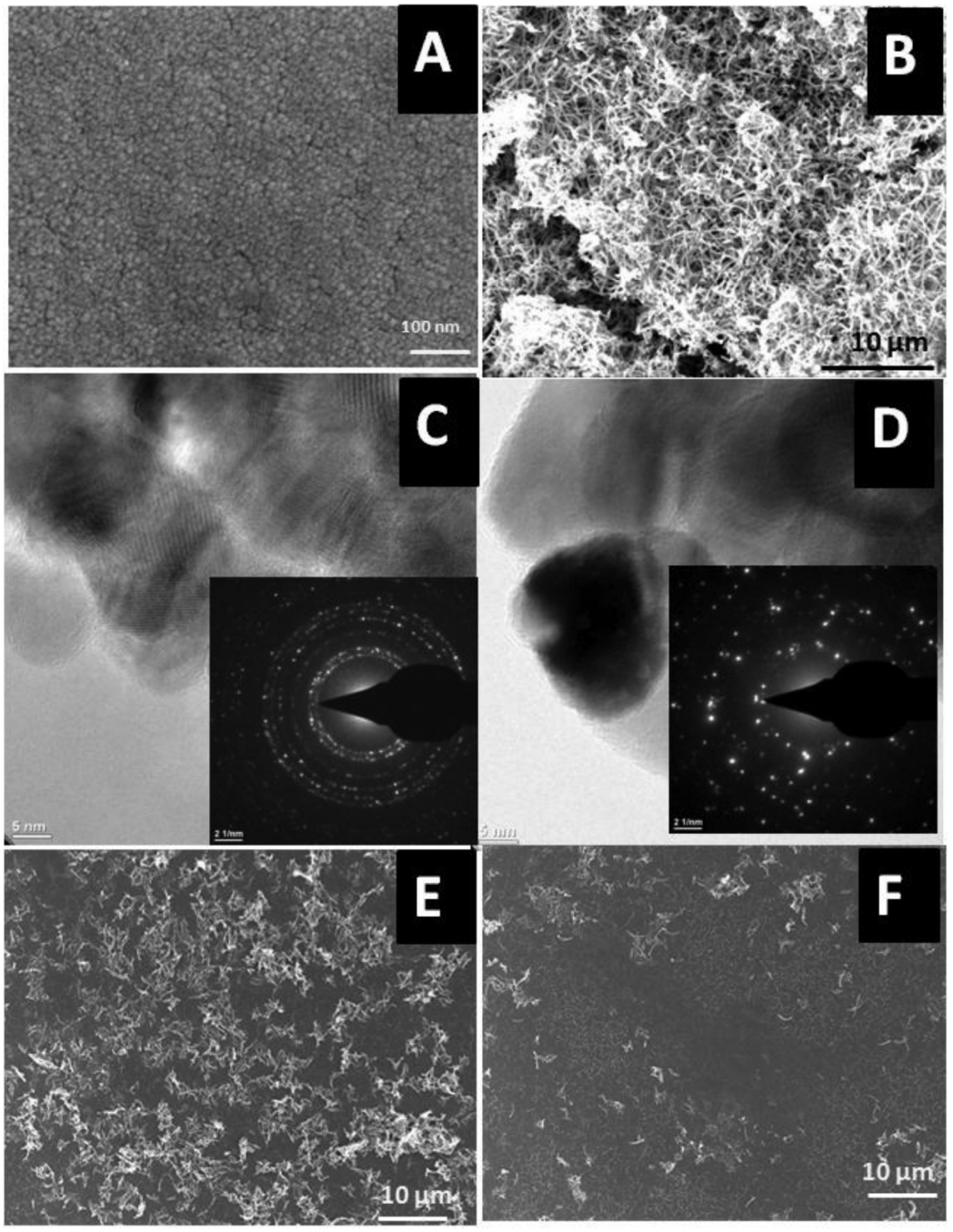

Figure 1. SEM images of (A) spin-coated sol−gel-derived ZnO nanoparticles, (B) electrospun ZnO nanofibers, (C) high-resolution TEM image of the ZnO nanoparticles. Inset shows the SAED pattern of the ZnO nanoparticle; (D) high-resolution TEM image of the ZnO nanowires. Inset shows the SAED pattern of the ZnO nanowires; (D) composite ZnO nanostructure combining ZnO nanoparticles and ZnO nanofibers (high conc.), (E) composite ZnO nanostructure combining ZnO nanoparticles and ZnO nanofibers (low conc.).

oscilloscope (1 MΩ) which allows measuring V_{OC} under variation of a white light illumination. A pulsed laser (wavelength: 532 nm, pulse width <5 ns, pulse repetition rate 1 Hz) was used to generate a small perturbation on V_{OC} (ΔV_{oc} < 20 mV). As the system is in open-circuit conditions, the voltage decay is proportional to the photogenerated excess carrier relaxation ($d\Delta V_{oc}/dt \propto d\Delta n/dt$) that allows measuring the carrier lifetime directly.

The carrier mobility and equilibrium carrier concentrations in the devices were measured by the charge extraction by linearly increasing voltage (CELIV) measurements. The CELIV measurement setup consists of a pulse generator (SRS-DG535), a digital oscilloscope (Agilent Infinium1 GHz) and a function generator (SRS-DG345). In Photo-CELIV, photogenerated carriers are produced by illuminating the sample using a pulsed laser (wavelength: 532 nm, pulse width <5 ns, pulse repetition rate 1 Hz) through the ITO side of the device. The delay dependence measurement is carried out by varying the time between the laser pulse and the voltage ramp.

The devices were encapsulated in a plastic encapsulant sealed with an epoxy resin for the CELIV measurements. The CELIV measurements were done in the dark by applying a linearly increasing voltage under reverse bias pulse with a slope of $A = V_{max}/t_{pulse}$. The voltage pulse width (t_{pulse}) was maintained at 20 μs and the amplitude (V_{max}) was varied from 0.5 to 3 V. When the reverse biased linearly increasing voltage ramp is applied to the device, the resultant output is obtained as a rectangular-shaped transient with a plateau corresponding to the capacitor displacement current (j_0) and the current (Δj) due to the

equilibrium carriers from the photoactive layer. The carrier mobility of the equilibrium charge carriers was evaluated using the relation $\mu = 2d^2/3At_{max}^2$; where d is the film thickness and t_{max} is the time taken to attain the maximum extraction current (J_{max}) and A is the rate of change of applied voltage for the extraction of charges.

3. RESULTS AND DISCUSSION

Figure 1 shows SEM images of ZnO films and wires developed in this study. ZnO film (Figure 1A) prepared by the sol−gel coating on ITO was smooth, continuous, and uniformly distributed spherical particles of diameter ∼10−20 nm. The SEM images of the electrospun ZnO nanowires in Figure 1B shows continuous wires of diameter ∼50−100 nm and few micrometers in length. Images C and D in Figure 1 show high-resolution TEM (HRTEM) images and SAED patterns of the ZnO particles and wires. The HRTEM images show that a typical powder particle of ∼20 nm is an aggregate of randomly oriented nanocrystals of sizes 2−5 nm whereas nanowires are composed of more oriented particles of size ∼10−20 nm, i.e., the nanowires are highly crystalline than the particles. The difference in their crystallinity is more obvious in the SAED patterns, both of which can be indexed for Wurtzite crystal structure (space group: $P6_3mc$). The SAED pattern of the particles show polycrystalline ring structures, whereas that of nanowires are spotty thereby indicating that they have improved crystallinity than the other. Figures 1E&F show the ZnO−PNW_L and ZnO−PNW_H films. The ZnO nanowires are broken down during the ultrasonic dispersion process and are distributed randomly in the composite film. Figure 2 shows the

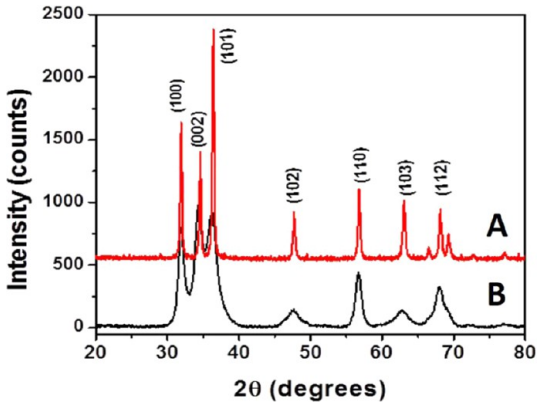

Figure 2. XRD spectra of (a) ZnO nanofibers (b) ZnO nanoparticles.

XRD patterns of the ZnO particulate and electrospun materials. The films were crystalline and all the XRD peaks can be indexed for the ZnO hexagonal phase with Wurtzite crystal structure [space group C6 V ($P6_3mc$)] having lattice parameters $a = b = 3.25$ Å and $c = 5.2$ Å (JCPDS card no. 0−3−0888).

Figure 3 summarizes the results of AFM studies on ZnO modified ITO. The root-mean-square (rms) roughness values of the ZnO modified ITO electrodes are 6.42, 54.3, and 113 nm for the devices P, PNW_L and PNW_H, respectively. The ZnO interlayer film thickness is in the range of about 20−45 nm for device P. The base thickness of the ZnO interlayer with nanowires in both PNW_L and PNW_H cases is similar to that of device P (20−45 nm). The nanowires are deposited randomly on top of this base layer; therefore, the surface height varied depending on the relative concentration of the nanowires at a spot. Surface heights of the PNW_L and PNW_H films were ∼150−350 nm and 400−700 nm, respectively.

Figure 4 shows the best current−voltage characteristics of the three types of devices at AM1.G conditions; and the average values ofphotovoltaic parameters are listed in Table 1. The device prepared using the ZnO−PNW films showed marginally higher short circuit current density (J_{SC}) and considerably higher fill factor (FF), which increased with increase in the nanowire loading. The FF determines the charge collection efficiency and recombination rate constant in solar cells; therefore, increase in nanowire concentration is beneficial for enhanced device performance. The J_{SC} values of devices P, PNW_L, and PNW_H were 9.1, 9, and 9.4 mA/cm^2, respectively. The open circuit voltage (V_{OC}) of the three devices remind at similar values (∼0.54 V). The device fabricated using the ZnO−PNW_H films gave the highest photoelectric conversion efficiency (PCE) of ∼3.5% which is 20% higher compared to the device that did not employ nanowire plantations which mainly resulted from 12% enhanced FF.

The difference in electrical property of the three types of devices was determined from the shunt (R_{SH}) and series (R_S) resistances from the inverse of slops at J_{SC} and V_{OC} of the $I-V$ curves, respectively. The R_{SH} is an estimation of internal currents in the device and is a measure of charge recombination processes whereas R_S denotes the resistance for charge collection.[38,39] A high R_{SH} (>1000 Ω) and low R_S (<100 Ω) are therefore preferred for high FF and PCE of IOSCs. Table 1 also includes the R_S and R_{SH} of the devices studied here. The R_S was lowest (∼77 Ω) for the device PNW_H among the various devices, which can be attributed to the improved charge collection efficiency when the nanoparticle/nanowire composite was employed as ETL in the device. Although all devices showed higher R_{SH} the device PNW_H showed ∼183% increased value (∼13826 Ω) compared to that of the device P (4883 Ω). The enhanced R_{SH} of the device PNW_H could be attributed to the enhanced charge transport because of the presence of one-dimensional materials and removal of shunt channels in the grain boundaries which otherwise existed in the devices. The observed lower R_S and doubled R_{SH} of the device PNW_H accounts for the considerable enhancement in its FF.

Incident photon-to-current conversion efficiency (IPCE) spectra of the devices "P", "PNW_L", and "PNW_H" are shown in Figure 5. The device PNW_H devices showed maximum IPCE of ∼68%, whereas that of the control device P was ∼62%. The measured IPCE integrated values are in good agreement with the short circuit current obtained from the $I-V$ measurements. A drop in IPCE at wavelengths around 400 nm with small increase in the UV region is clearly evident in all three devices because of absorption of the buffer layer film corresponding to the band edge of ZnO. Interestingly, the devices incorporating ZnO plantations showed a peak ∼450 nm, which was not observed in the other device. This observation indicates that the blend layer morphology including the charge carrier percolation networks are altered beneficially via the incorporation of the ZnO NWs by improved phase separation. Furthermore, the spectra of the nanowire planted devices showed an increase in quantum efficiency in the 450−650 nm range; thereby indicating a scattering-induced absorption enhancement in the photoactive layer. The improved vertical phase segregation of the photoactive layer by ZnO NWs has resulted in increased IPCE of ∼58% compared to 45% in device P at 450 nm.

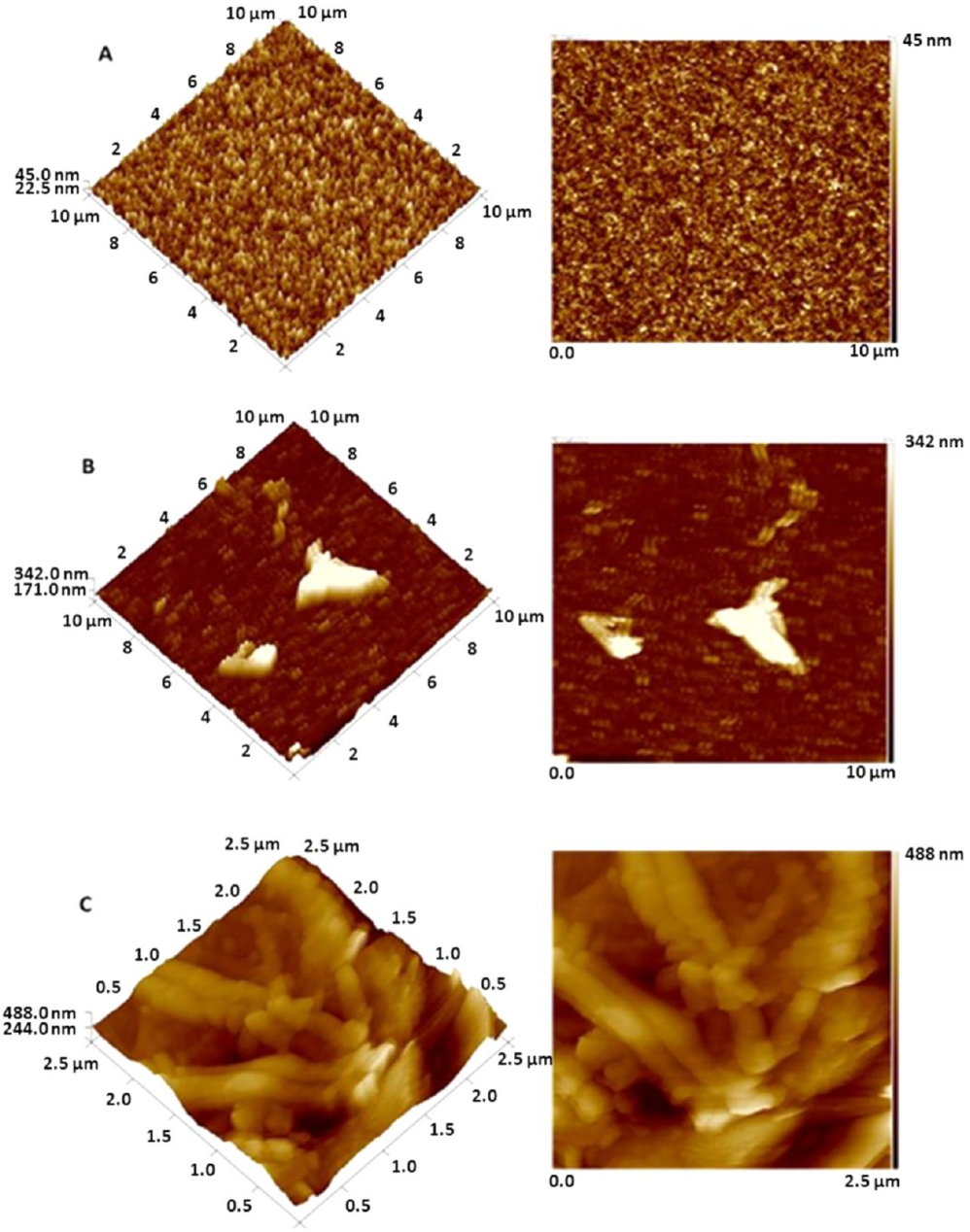

Figure 3. AFM images of the ZnO interlayer in devices (A) P, (B) PNW_L, and (C) PNW_H, respectively. Images in the left represents the 3D view depicting the surface height and the images (right) represents the 2D view of the nanostructure morphology.

To investigate the role of recombination dynamics on the enhanced photovoltaic action of the devices employing ZnO nanowires, we extracted the carrier lifetime (τ_n) from TPV measurements by back-side illumination. The photovoltage decay was measured by keeping the device at a reference voltage well below the V_{OC} and creating an additional photovoltage using a short laser pulse (~30 mV). The decay time of the additional photovoltage is therefore a measure of recombination time and is monitored in the TPV measurements. i.e., the longer is the photovoltage decay time the longer is the carrier lifetime; and therefore, longer photovoltage decay time represents reduced charge recombination.[20] Figure 6a compares typical photovoltage transients recorded at a steady-state using a white light of reference photovoltage ~240 mV for all the three devices. One may easily observe from the Figure 6a that the photovoltage of the device employing a higher concentration of electrospun ZnO nanowires, i.e., device PNW_L, decays much slower compared to the other two devices thereby indicating higher carrier lifetime and reduced charge recombination.

Assuming a first order decay, the τ_n was calculated from the TPV decay using the equation[20]

$$\tau_n = \left(\frac{\partial U_n}{\partial_n}\right)^{-1}_n \quad (1)$$

where U_n is the electron recombination rate per unit volume and n is the carrier concentration, respectively. The τ_n of devices P, PNW_L, and PNW_H at a reference photovoltage of 240 mV were calculated to be 0.202, 0.294, and 0.771 ms respectively. Thus, clearly, carrier recombination is over three times slower in the device PNW_H compared to other devices;

dx.doi.org/10.1021/am4013853 | ACS Appl. Mater. Interfaces 2013, 5, 9396−9404

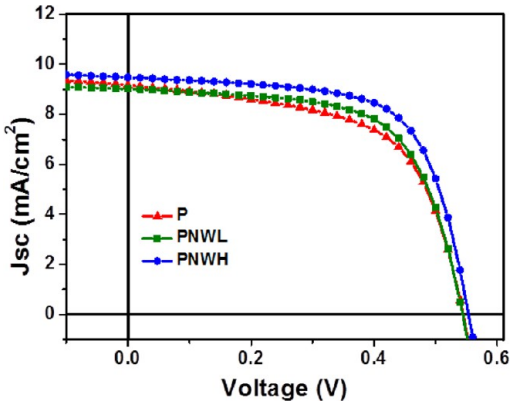

Figure 4. Current density–voltage characteristics of devices P, PNW_L, and PNW_H.

Table 1. The photovoltaic parameters of the three types of devices. Average values from three devices are listed in each type

device	J_{SC} (mA/cm^2)	V_{OC} (V)	FF (%)	PCE (%)	R_S (Ω)	R_{SH} (Ω)
P	9.1	0.54	59.7	2.9	84.1	4883
PNW_L	9.0	0.54	64.1	3.1	80.5	10320
PNW_H	9.4	0.55	66.1	3.5	77.4	13826

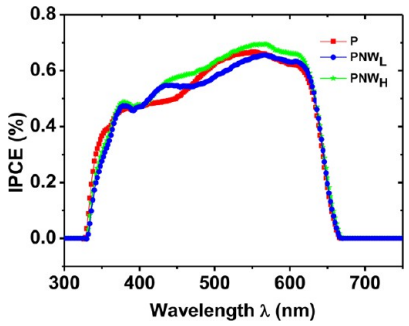

Figure 5. IPCE spectra of the devices P, PNW_L, and PNW_H.

therefore, a higher FF could normally be expected from this device.

The τ_n in OSCs depends strongly on its working conditions. At V_{OC}, with maximum band bending, the traps in the photoactive layer are filled up and a bimolecular recombination mechanism operates involving both types of carriers.[40,41] Carriers are short-lived under such condition.[41] However, below V_{OC}, with lesser band bending, the traps above the Fermi level are no longer filled and a monomolecular recombination mechanism operates involving one type of carrier with the other being in the trap.[42] Carriers are comparatively longer lived in this condition and a difference in the extraction efficiency by the ETL is more pronounced.[20] The photovoltage decay transients obtained for the three types of device at the V_{oc} ≈ 240 mV is shown in Figure 6a. The decay time was longer for the device with high concentration of nanowires (PNW_H) compared to P and PNW_L, which can be observed clearly from figure 6a. The carrier lifetime τ_n values calculated from the decay transients (Figure 6a) measured at Voc~240 mV are shown in figure 6b (encircled) indicating a profound increase in carrier lifetime for device PNW_H. Similarly, the variation of τ_n at its respective photovoltages (V_{OC}) for the three types of devices is shown in figure 6b. In all the three types of devices, the τ_n is of the order of microseconds at the higher photovoltage whereas it increases to milliseconds at lower photovoltages. At maximum V_{OC}, the similarity in the τ_n of the devices implies that charge transport across the ETL is not influenced by its morphology. Interestingly, the τ_n showed a large variation among the devices for $V_{OC} \leq 400$ mV. The τ_n of device PNW_H is an order of magnitude higher compared to the other devices for $V_{OC} \leq 200$ mV which imply that the electrospun ZnO nanowires collect electrons from the bulk of the photoactive layer, i.e., the one-dimensional nanowires plantations offer more charge collection points at the ZnO-PCBM interface thereby facilitating faster removal electrons through the ETL, increases carrier lifetime, and FF.

To corroborate long recombination time in the device PNW_H, delay-dependent photo-CELIV transients of the devices were recorded and analyzed. Rationale of this experiment is that carriers in devices of higher carrier lifetime can still be extracted even after considerable delay time after the light pulse.[43] Figure 7 shows the normalized charge carrier concentration (n) obtained from the delay dependent photo-CELIV transients (see the Supporting Information). About 40% of the total carriers are extracted even after an extended time delay of 50 μs in the device PNW_H. The other two devices showed extraction of comparatively lower fraction of carriers at such delay times thereby indicating lower recombination time.

The CELIV transients obtained for the three devices P, PNW_L, and PNW_H is shown in Figure 8a. The CELIV technique directly measures the μ in materials with dispersive transport. In the CELIV technique, a linearly increasing electric

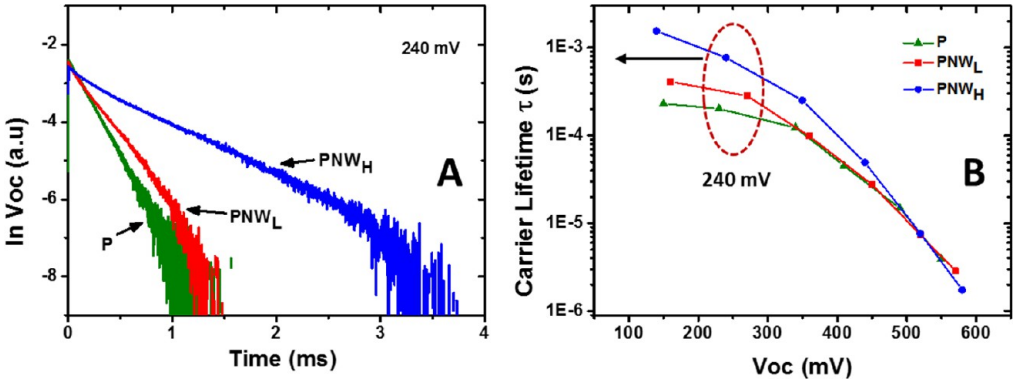

Figure 6. (A) Photovoltage decay transients recorded at 240 mV; (B) carrier lifetime calculated from TPV measurements.

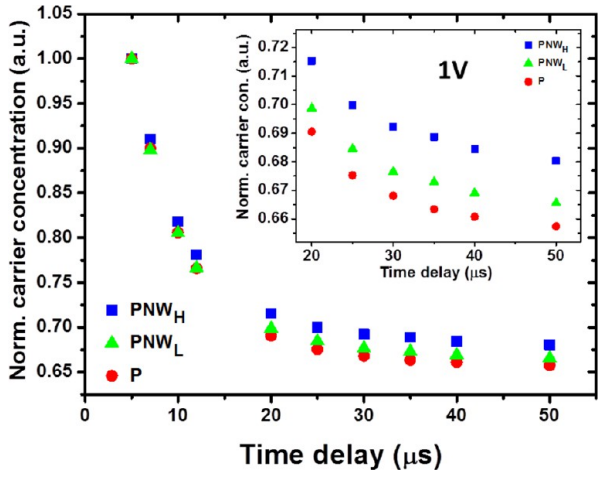

Figure 7. Normalized drop in carrier concentration (n) as a function of time delay obtained from the delay-dependent photo-CELIV transients. (Inset) Enlarged view of drop in carrier concentration (20–50 ms) as a function of time delay.

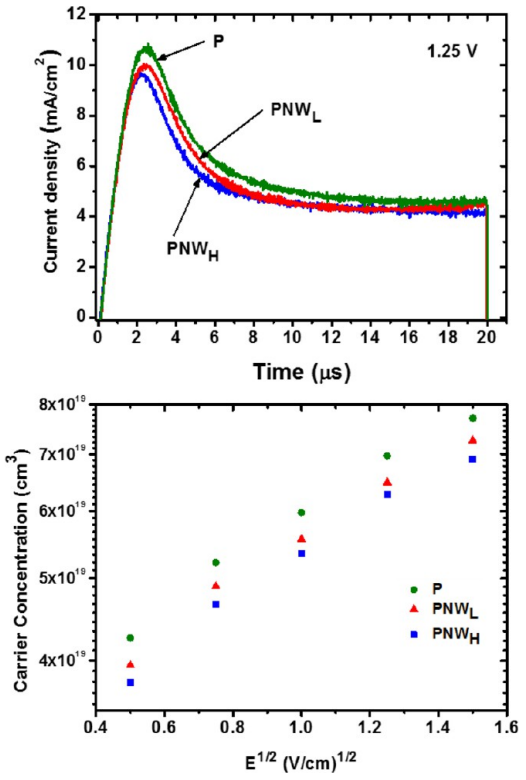

Figure 8. (A) CELIV (Dark) transients of the devices P, PNW_L, and PNW_H measured at 1.25 V with an offset of 0.25 V. (B) Equilibrium charge carrier concentration obtained from CELIV transients at different applied field.

field or voltage ramp is applied at one of the contacts under reverse bias condition and the corresponding current transients is used to determine the injected dark carriers and equilibrium carrier concentration n.[43,44] CELIV technique also enables the analysis of the relaxation process of the charge carriers in the density of states (DOS) thereby facilitating simultaneous measurement of time-dependent μ and n.[22,45] In general, a device with less dark injection or leakage current at reverse bias condition is suitable for charge extraction measurements as well as to reduce the charge recombination in the operational device. The difference in the heights of the characteristic peak (J_{max}) of the CELIV transients, as observed in Figure 8a, depicts that the dark injection is lesser in the device PNW_H whereas it is relatively higher in the device without nanowires P. In addition, the time taken to reach the steady state or capacitance displacement current is shorter in the nanowire-based device (PNW_H) compared to the devices without nanowires. The small injection current in PNW_H based device may indicate that the charge recombination probability in this device is smaller compared to the other two devices. In addition, the width of the CELIV transient indicates the charge dispersion in the system. It was observed that the PNW_H-based device, the width is smaller compared to the other two devices indicating the good charge transport characteristics. The variation of dark injected carrier concentration as a function of applied field (reverse bias) is shown in Figure 8b. It can be seen that the dark carrier injection is consistently lesser in PNW_H compared to its counterparts PNW_L and P, respectively (figure 8b). These results indicate that the device incorporating nanowires enables efficient charge extraction across the ETL whereas they are accumulated in devices without nanowires. Lowering of the charge accumulation at the interface via efficient electron collection pathways in the "PNW" devices is the key for improved shunt resistance as shown in Table 1.

Figure 9 shows the carrier mobility obtained from the CELIV transients. The μ gradually increased with increase in the

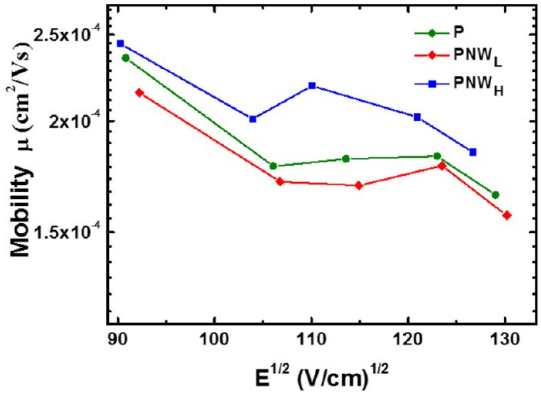

Figure 9. Charge carrier mobility obtained from the CELIV transients.

nanowire concentration although the magnitude of this increment was not substantial. It denotes that the improved device performance arise from increased carrier lifetime when the nanowire plantations directly collects electrons from the bulk of the photoactive layer. In the absence of the nanowires, longer transport time to the charge transport layers eventually lead to recombination and subsequent lowering of PCE.

CONCLUSIONS

In conclusion, we have employed electrospun ZnO nanowire plantations in the electron transporting layer of inverted organic solar cells and found that the resulting device show enhanced photovoltaic performance. The devices structure was ITO/ZnO/P3HT:PCBM/MoO_3/Ag. Three types of devices were fabricated with varying nanowire concentration; the one without the nanowires was used as a control device. The devices that employed a higher loading of ZnO nanowires showed 20% higher photoelectric conversion efficiency which mainly resulted from considerable enhancement in fill factor. Transient photovoltage decay and charge extraction by linearly

increasing voltage measurements show that electrons are collected from the bulk of the photoactive layer by the nanowire plantations in devices that employed them. Such collection lowered the electron diffusion length (or diffusion pathways); and therefore, charges could be collected efficiently. On the other hand, in the control device, the electrons are required to diffuse until a flat photoactive−electron transport layer interface which increased the diffusion length; and therefore an enhanced recombination rate. Thus, the nanowire plantations efficiently reduced recombination rate and improved the photoelectric performance parameters.

■ ASSOCIATED CONTENT

Supporting Information

The delay-dependent CELIV transients recorded for time delays between 5 and 50 μs for the P, PNW_L, and PNW_H devices. This material is available free of charge via the Internet at http://pubs.acs.org/.

■ AUTHOR INFORMATION

Corresponding Authors

*E-mail: c-vijila@imre.a-star.edu.sg.
*E-mail: rjose@ump.edu.my.

Author Contributions

†Authors N.K.E. and T.M.J. contributed equally to this work

Notes

The authors declare no competing financial interest.

■ ACKNOWLEDGMENTS

NK.E. acknowledges the Institute of Materials Research and Engineering (IMRE) and the Mechanical Engineering Department of National University of Singapore for providing research support and scholarship for the work. This project is supported by A-STAR-JST Strategic International Cooperative Programme (first joint grant call project number 1021630071). R.J. acknowledges the MTUN-CoE grant for solar cloths.

■ REFERENCES

(1) Xue, J. *Polym. Rev.* **2010**, *50*, 411−419.
(2) Krebs, F. C. *Org. Electron.* **2009**, *10*, 761−768.
(3) Alstrup, J.; Norrman, K.; Jørgensen, M.; Krebs, F. C. *Sol. Energy Mater. Sol. Cells* **2006**, *90*, 2777−2792.
(4) De Leeuw, D. M.; Simenon, M. M. J.; Brown, A. R.; Einerhand, R. E. F. *Synth. Met.* **1997**, *87*, 53−59.
(5) Blouin, N.; Michaud, A.; Gendron, D.; Wakim, S.; Blair, E.; Neagu-Plesu, R.; Belletête, M.; Durocher, G.; Tao, Y.; Leclerc, M. *J. Am. Chem. Soc.* **2008**, *130*, 732−742.
(6) Yella, A.; Lee, H.-W.; Tsao, H. N.; Yi, C.; Chandiran, A. K.; Nazeeruddin, M. K.; Wei-Guang Diau, E.; Yeh, C.-Y.; Zakeeruddin, S. M.; Grätzel, M. *Science* **2011**, *334*, 629.
(7) Ibrahem, M. A.; Wei, H.-Y.; Tsai, M.-H.; Ho, K.-C.; Shyue, J.-J.; Chu, C. W. *Sol. Energy Mater. Sol. Cells* **2013**, *108*, 156−163.
(8) Chen, L. M.; Hong, Z.; Li, G.; Yang, Y. *Adv. Mater.* **2009**, *21*, 1434−1449.
(9) Manor, A.; Katz, E. A.; Tromholt, T.; Krebs, F. C. *Adv. Energy Mater.* **2011**, *1*, 836−843.
(10) Hau, S.; Yip, H.-L.; Jen, A. *Polym. Rev.* **2010**, *50*, 474−510.
(11) Kyaw, A. K. K.; Sun, X. W.; Jiang, C. Y.; Lo, G. Q.; Zhao, D. W.; Kwong, D. L. *Appl. Phys. Lett.* **2008**, *93*, 221107.
(12) Zhao, D. W.; Liu, P.; Sun, X. W.; Tan, S. T.; Ke, L.; Kyaw, A. K. K. *Appl. Phys. Lett.* **2009**, *95*, 153304.
(13) Zhao, D. W.; Tan, S. T.; Ke, L.; Liu, P.; Kyaw, a. K. K.; Sun, X. W.; Lo, G. Q.; Kwong, D. L. *Sol. Energy Mater. Sol. Cells* **2010**, *94*, 985−991.
(14) Zhao, D. W.; Tan, S. T.; Ke, L.; Liu, P.; Kyaw, A. K. K.; Sun, X. W.; Lo, G. Q.; Kwong, D. L. *Sol. Energy Mater. Sol. Cells* **2010**, *94*, 985−991.
(15) Steim, R.; Kogler, F. R.; Brabec, C. J. *J. Mater. Chem.* **2010**, *20*, 2499−2499.
(16) Po, R.; Carbonera, C.; Bernardi, A.; Camaioni, N. *Energy Environ. Sci.* **2010**, *4*, 285−310.
(17) Kang, Y. J.; Lim, K.; Jung, S.; Kim, D.-G.; Kim, J. K.; Kim, C. S.; Kim, S. H.; Kang, J. W. *Sol. Energy Mater. Sol. Cells* **2012**, *96*, 137−140.
(18) Bai, S.; Wu, Z.; Xu, X.; Jin, Y.; Sun, B.; Guo, X.; He, S.; Wang, X.; Ye, Z.; Wei, H.; Han, X.; Ma, W. *Appl. Phys. Lett.* **2012**, *100*, 203906−203906.
(19) Hu, Z.; Zhang, J.; Liu, Y.; Hao, Z.; Zhang, X.; Zhao, Y. *Sol. Energy Mater. Sol. Cells* **2011**, *95*, 2126−2130.
(20) Boix, P. P.; Ajuria, J.; Pacios, R.; Garcia-Belmonte, G. *J. Appl. Phys.* **2011**, *109*, 074514−074514.
(21) Gwinner, M. C.; Vaynzof, Y.; Banger, K. K.; Ho, P. K. H.; Friend, R. H.; Sirringhaus, H. *Adv. Funct. Mater.* **2010**, *20*, 3457−3465.
(22) Pivrikas, A.; Sariciftci, N. S.; Juška, G.; Osterbacka, R. *Prog. Photovol. Res. Appl.* **2007**, *15*, 677−696.
(23) Archer, M. D.; Nozik, A. J. *Nanostructured and Photoelectrochemical Systems for Solar Photon Conversion*; Imperial College Press: London, 2008.
(24) Brédas, J.-L.; Beljonne, D.; Coropceanu, V.; Cornil, J. *Chem. Rev.* **2004**, *104*, 4971−5004.
(25) Elumalai, N. K.; Saha, A.; Vijila, C.; Jose, R.; Jie, Z.; Ramakrishna, S. *Phys. Chem. Chem. Phys.* **2013**, *15*, 6831−6841.
(26) Mbule, P. S.; Kim, T. H.; Kim, B. S.; Swart, H. C.; Ntwaeaborwa, O. M. *Sol. Energy Mater. Solar Cells* **2013**, *112*, 6−12.
(27) Liang, Z.; Zhang, Q.; Wiranwetchayan, O.; Xi, J.; Yang, Z.; Park, K.; Li, C.; Cao, G. *Adv. Funct. Mater.* **2012**, *22*, 2194−2201.
(28) Yang, X.; Loos, J.; Veenstra, S. C.; Verhees, W. J. H.; Wienk, M. M.; Kroon, J. M.; Michels, M. A. J.; Janssen, R. A. J. *Nano Lett.* **2005**, *5*, 579−583.
(29) Wang, M.; Li, Y.; Huang, H.; Peterson, E. D.; Nie, W.; Zhou, W.; Zeng, W.; Huang, W.; Fang, G.; Sun, N.; Zhao, X.; Carroll, D. L. *Appl. Phys. Lett.* **2011**, *98*, 103305−103305.
(30) Gonzalez-Valls, I.; Lira-Cantu, M. *Energy Environ. Sci.* **2009**, *2*, 19−34.
(31) Zhang, Q.; Yodyingyong, S.; Xi, J.; Myers, D.; Cao, G. *Nanoscale* **2012**, *4*, 1436.
(32) Archana, P. S.; Naveen Kumar, E.; Vijila, C.; Ramakrishna, S.; Yusoff, M. M.; Jose, R. *Dalton Trans.* **2013**, *42*, 1024−1032.
(33) Kumar, E. N.; Jose, R.; Archana, P. S.; Vijila, C.; Yusoff, M. M.; Ramakrishna, S. *Energy Environ. Sci.* **2012**, *5*, 5401−5407.
(34) Elumalai, N. K.; Jose, R.; Archana, P. S.; Chellappan, V.; Ramakrishna, S. *J. Phys. Chem. C* **2012**, *116*, 22112−22120.
(35) Archana, P. S.; Jose, R.; Yusoff, M. M.; Ramakrishna, S. *Appl. Phys. Lett.* **2011**, *98*, 152106.
(36) Archana, P. S.; Jose, R.; Vijila, C.; Ramakrishna, S. *J. Phys. Chem. C* **2009**, *113*, 21538−21542.
(37) Ramakrishna, S.; Jose, R.; Archana, P. S.; Nair, A. S.; Balamurugan, R.; Venugopal, J.; Teo, W. E. *J. Mater. Sci.* **2010**, *45*, 6283−6312.
(38) Fabregat-Santiago, F.; Bisquert, J.; Palomares, E.; Otero, L.; Kuang, D.; Zakeeruddin, S. M.; Grätzel, M. *J. Phys. Chem. C* **2007**, *111*, 6550−6560.
(39) Fabregat-Santiago, F.; Bisquert, J.; Garcia-Belmonte, G.; Boschloo, G.; Hagfeldt, A. *Sol. Energy Mater. Solar Cells* **2005**, *87*, 117−131.
(40) Cowan, S. R.; Roy, A.; Heeger, A. J. *Phys. Rev. B* **2010**, *82*, 245207−245207.
(41) Koster, L. J. a.; Mihailetchi, V. D.; Blom, P. W. M. *Appl. Phys. Lett.* **2006**, *88*, 052104−052104.
(42) Petersen, A.; Kirchartz, T.; Wagner, T. *Phys. Rev. B* **2012**, *85*, 1−11.
(43) Dennler, G.; Mozer, A.; Juska, G.; Pivrikas, A.; Osterbacka, R.; Fuchsbauer, A.; Sariciftci, N. *Org. Electron.* **2006**, *7*, 229−234.

(44) Tiwari, S.; Greenham, N. C. *Opt. Quantum Electron.* **2009**, *41*, 69−89.
(45) Genevičius, K.; Österbacka, R.; Juška, G.; Arlauskas, K.; Stubb, H. *Thin Solid Films* **2002**, *403*, 415−418.